Design and Development of High-Performance Composites for Enhanced Bridge Durability

Final Report
October 2025

Principal Investigator: Sumanta Das

Civil and Environmental Engineering
University of Rhode Island

Authors
Bolaji Oladipo; Domenico Simari and Sumanta Das

Sponsored By
Transportation Infrastructure Durability Center

A report from
University of Rhode Island
Civil and Environmental Engineering
2 E Alumni Ave, Kingston, RI 02881
Phone: 401-874-5637
Website: https://web.uri.edu/cve/

THE UNIVERSITY OF MAINE · UMASS LOWELL · WESTERN NEW ENGLAND UNIVERSITY WNE · UCONN · THE UNIVERSITY OF RHODE ISLAND · The UNIVERSITY of VERMONT

About the Transportation Infrastructure Durability Center

The Transportation Infrastructure Durability Center (TIDC) is the 2018 US DOT Region 1 (New England) University Transportation Center (UTC) located at the University of Maine Advanced Structures and Composites Center. TIDC's research focuses on efforts to improve the durability and extend the life of transportation infrastructure in New England and beyond through an integrated collaboration of universities, state DOTs, and industry. The TIDC is comprised of six New England universities, the University of Maine (lead), the University of Connecticut, the University of Massachusetts Lowell, the University of Rhode Island, the University of Vermont, and Western New England University.

U.S. Department of Transportation (US DOT) Disclaimer

The contents of this report reflect the views of the authors, who are responsible for the facts and the accuracy of the information presented herein. This document is disseminated in the interest of information exchange. The report is funded, partially or entirely, by a grant from the U.S. Department of Transportation's University Transportation Centers Program. However, the U.S. Government assumes no liability for the contents or use thereof.

Acknowledgements

Funding for this research is provided by the Transportation Infrastructure Durability Center at the University of Maine under grant 69A3551847101 from the U.S. Department of Transportation's University Transportation Centers Program.

Technical Report Documentation Page

1. Report No.	**2. Government Accession No.**	**3. Recipient Catalog No.**
4 Title and Subtitle Design and Development of High-Performance Composites for Improved Durability of Bridges in Rhode Island		**5 Report Date 10/17/2025** **6 Performing Organization Code**
7. Author(s) Bolaji Oladipo https://orcid.org/0000-0002-8032-3832 Domenico Simari Sumanta Das https://orcid.org/0000-0001-5339-7708		**8 Performing Organization Report No.**
9 Performing Organization Name and Address University of Rhode Island, 45 Upper College Rd, Kingston, RI 02881		**10 Work Unit No. (TRAIS)** **11 Contract or Grant No.**
12 Sponsoring Agency Name and Address U.S. Department of Transportation		**13 Type of Report and Period Covered** **14 Sponsoring Agency Code**

15 Supplementary Notes

16 **Abstract:** The deterioration of structural components within the nation's transportation infrastructure has long been a major concern. This project developed and evaluated 3D-printed composite materials as practical solutions for structural strengthening and rehabilitation. The work focused on several approaches, including sandwich composites with 3D-printed cores and fiber-reinforced polymer (FRP) systems with tailored 3D-printed architectures designed to improve strength and durability. These materials were assessed for their structural performance, adaptability, and potential for use in repairing and strengthening existing components of transportation infrastructure. Results from material characterization, mechanical testing, and predictive modeling confirmed that 3D-printed composite systems can provide reliable and efficient options for improving the performance of degraded structures. The findings contribute to a better understanding of how advanced manufacturing techniques can support durable and cost-effective solutions for infrastructure maintenance and renewal.

17 Key Words		**18 Distribution Statement** No restrictions. This document is available to the public through	
19 Security Classification (of this report) Unclassified	**20 Security Classification (of this page)** Unclassified	**21 No. of pages**	**22 Price**

Form DOT F 1700.7 (8-72)

Contents

List of Figures

List of Tables

List of Key Terms

Auxetic Material:
A material that exhibits a negative Poisson's ratio—expanding laterally when stretched and contracting laterally when compressed. This unusual behavior enhances confinement and crack control in structural applications.

Re-entrant Honeycomb (3RE) Geometry:
A type of auxetic structure characterized by inward-angled cell walls. The re-entrant design enables lateral expansion under tension and improved energy absorption under compression, making it effective for concrete confinement.

Continuous Carbon Fiber (CCF):
High-strength, lightweight fibers embedded within the TPU matrix to enhance stiffness and load-carrying capacity. CCF reinforcement improves the overall mechanical performance of the auxetic core.

Carbon Fiber Reinforced Polymer (CFRP):
A composite material composed of carbon fibers embedded in a polymer matrix, used as an external confinement layer. CFRP wraps significantly increase compressive strength and ductility in reinforced concrete structures.

Finite Element Analysis (FEA):
A computational method used to simulate the mechanical response of materials and structures under load. FEA was used to model stress distribution, confinement efficiency, and deformation behavior across scales.

Negative Poisson's Ratio (NPR):
A measure of auxetic behavior, indicating that a material expands laterally when stretched. NPR materials offer enhanced energy absorption and damage tolerance compared to conventional positive-Poisson-ratio materials.

Confinement Efficiency:
A measure of how effectively a surrounding material or composite system restrains lateral expansion and delays cracking in concrete under compression. High confinement efficiency translates to improved strength and ductility.

Abstract

The deterioration of structural components within the nation's transportation infrastructure has long been a major concern. This project developed and evaluated 3D-printed composite materials as practical solutions for structural strengthening and rehabilitation. The work focused on several approaches, including sandwich composites with 3D-printed cores and fiber-reinforced polymer (FRP) systems with tailored 3D-printed architectures designed to improve strength and durability. These materials were assessed for their structural performance, adaptability, and potential for use in repairing and strengthening existing components of transportation infrastructure. Results from material characterization, mechanical testing, and predictive modeling confirmed that 3D-printed composite systems can provide reliable and efficient options for improving the performance of degraded structures. The findings contribute to a better understanding of how advanced manufacturing techniques can support durable and cost-effective solutions for infrastructure maintenance and renewal.

Chapter 1: Introduction and Background

1.1 Project Motivation

Infrastructure forms the backbone of the nation's economy, supporting mobility, commerce, and overall quality of life. However, the continued deterioration of transportation infrastructure across the country has raised serious concerns regarding safety, service reliability, and long-term economic impact. While progress has been made in recent years through targeted investment and rehabilitation programs, the overall condition of many structural components remains below desired levels.

In Rhode Island and other northeastern states, maintaining and improving the condition of transportation infrastructure remains a pressing challenge due to aging assets and harsh environmental conditions. These challenges highlight the need for durable materials, innovative construction technologies, and efficient repair strategies that can extend the service life of critical structural systems.

The motivation for this project arises from the need to address these persistent issues through research and development of advanced composite materials and modern strengthening methods. By developing and implementing new material systems with enhanced performance and durability, this work contributes toward creating a more resilient, sustainable, and long-lasting transportation infrastructure network.

1.2 Research, Objectives, and Tasks

The overall objective of this project was to design, develop, and evaluate advanced 3D-printed composite systems for the structural strengthening and rehabilitation of transportation infrastructure. The work focused on creating durable and efficient materials capable of improving performance and extending the service life of degraded concrete components.

To accomplish this objective, the project involved several related tasks. The first task focused on the design of re-entrant honeycomb cores with auxetic behavior to enhance energy absorption and strength recovery. Numerical simulations and machine learning techniques were used to study the effects of geometry and material configuration on structural performance and manufacturability.

The next task involved fabricating the designed 3D-printed auxetic cores and integrating them with degraded concrete cylinders. These strengthened specimens were subjected to a comprehensive mechanical performance assessment to evaluate their overall strengthening effectiveness and durability.

Subsequent tasks included conducting numerical simulations to analyze the behavior of auxetic cores wrapped around concrete cylinders and to study their structural response under service conditions. Continuous carbon fibers and fiber-reinforced polymer (FRP) plates were incorporated in a sandwich configuration around the cores to enhance strength and load-carrying capacity. Additional simulations were carried out to assess the performance of these multi-layered strengthening systems.

1.3 Report Overview

This report documents the design, development, and evaluation of 3D-printed composite systems incorporating re-entrant honeycomb cores for the structural strengthening and rehabilitation of transportation infrastructure. It presents the methodology used to design and fabricate auxetic core geometries, along with the mechanical performance assessment of concrete cylinders strengthened using these 3D-printed composites. The report also describes the simulation and machine learning approaches developed to study the structural response of auxetic cores and composite configurations under various loading and service conditions. The results and their interpretations are discussed in detail, highlighting the relationships between material geometry, mechanical behavior, and strengthening performance. The report concludes with key findings, recommendations for practical application, and directions for future research to support the broader adoption of 3D-printed composite systems in infrastructure strengthening and rehabilitation.

Chapter 2: Methodology

2.1 Design and Mechanical Evaluation of Auxetic Structures

Geometry Generation and Modeling

Re-entrant honeycomb auxetic geometries were generated using a Python-based parametric modeling script that defined geometric parameters including vertical and slant cell lengths, wall thickness, and re-entrant angle. A representative model with specified geometry was created and imported into Abaqus CAE for finite element analysis (FEA).

Finite Element Analysis Setup

Finite element analysis was performed to study the deformation and Poisson's ratio behavior of the auxetic geometries under uniaxial tension. Quadrilateral-dominant CPE4H elements were used for meshing, with curvature control applied to capture the small-radius features of the structure. One end of the model was fixed while the opposite end was subjected to a controlled displacement load. The resulting deformation field is shown in Fig. 1. MATLAB-based post-processing was used to compute strains and Poisson's ratios from the simulated displacements.

Fabrication and Experimental Testing

The optimized auxetic geometries were fabricated using fused filament fabrication (FFF) on a Creality CR-10 V3 3D printer with Overture™ thermoplastic polyurethane (TPU) filament. Printing was performed at a nozzle temperature of 225°C, bed temperature of 50°C, and print speed of 30 mm/s with 100% infill. The layer thickness was maintained at 0.2 mm to ensure consistent interlayer bonding. Each printed specimen was coated with a fine black–white speckle pattern using acrylic paint to enable digital image correlation (DIC). The surface speckle density was adjusted to yield a spatial resolution of approximately 3 × 3 pixels per speckle. Uniaxial tensile testing was performed using a 10 kN Shimadzu Autograph AGS-X universal testing machine under a displacement rate of 2 mm/min at room temperature (25°C). A FLIR Blackfly S camera captured one image per second during loading, generating a sequence of 596 images per test. These images were processed in VIC-2D software to compute full-field displacements and strains, as illustrated

in Fig. 2. The DIC results provided direct validation of the FEA-predicted deformation and Poisson's ratio, confirming the auxetic expansion behavior and establishing a foundation for the next phase of integration with cementitious materials.

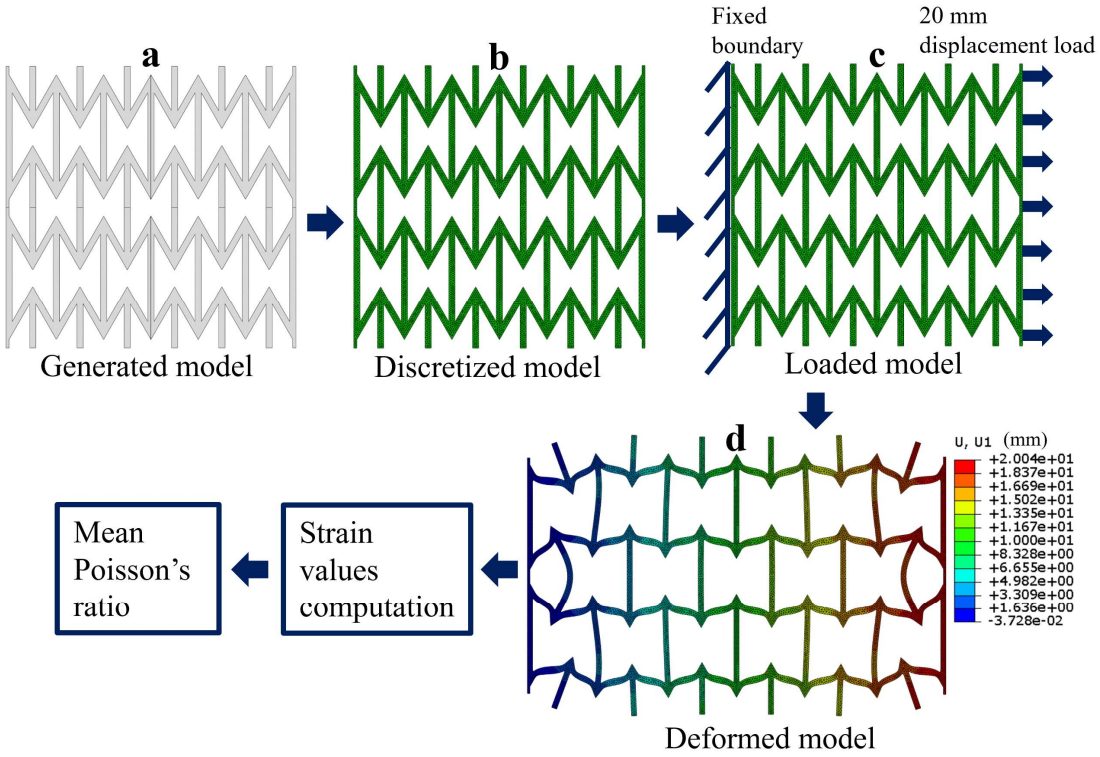

Fig. 1 - Schematic representation of the FEA simulation framework. From left to right, (a) the model generated from the Python script followed by (b) the TRI/QUAD discretized model, (c) the loaded model, and (d) the deformed model of the FEA with a color spectrum showing the maximum displacement tensile load of 20 mm.

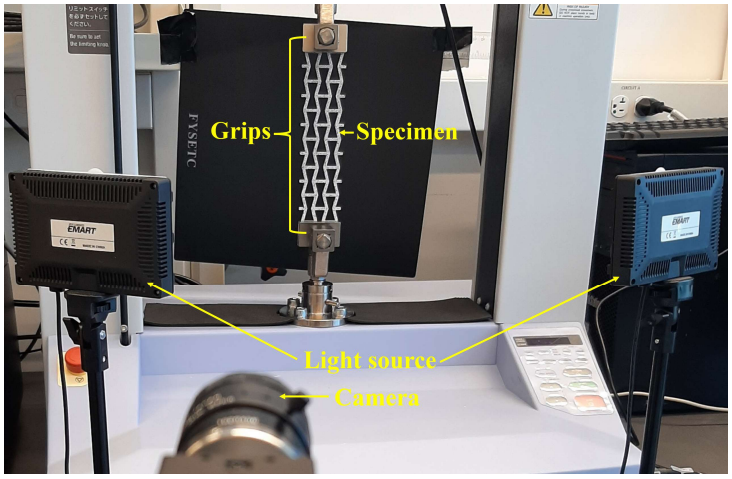

Fig. 2 - 2D DIC setup of a selected sample geometry.

2.2 Fabrication and Testing of Cementitious Specimens with Auxetic Cores

Mortar Mix Preparation

Cementitious mortar specimens were prepared with a 50% paste volume fraction to maintain a balanced paste-to-sand ratio. The water-to-cement ratio (w/c) was maintained at 0.4 to ensure uniform workability and strength development. The mix design followed standard ASTM C305 procedures. The mortar was cast into cylindrical molds and vibrated to minimize air entrapment. After demolding at 24 hours, specimens were cured in water for 28 days to achieve full hydration and stable mechanical properties.

Integration of Auxetic Cores

Re-entrant auxetic cells were designed with variable geometry by adjusting cell thickness, base length, and re-entrant angle. Auxetic cores were fabricated using PLA, ABS, and TPU to evaluate the effect of material stiffness and geometry on confinement behavior. The printed auxetic wraps were carefully fitted around cured mortar cylinders to form composite confined specimens. The final integrated assemblies are illustrated in Fig. 3.

Fig. 3 — Representative re-entrant auxetic cores and integration around mortar cylinders

Mechanical Evaluation

Uniaxial compression tests were conducted to determine the compressive strength of the auxetic-confined mortar specimens. Cylindrical specimens were tested under load control using a servo-hydraulic universal testing machine equipped with a calibrated load cell. Each specimen was placed concentrically between the machine platens to ensure uniform load distribution and to minimize eccentricity during testing. A constant loading rate was maintained throughout the test until specimen failure. The applied load was continuously recorded, and the compressive strength was calculated by dividing the maximum load at failure by the cross-sectional area of the specimen. For each auxetic configuration, multiple specimens were tested to ensure consistency and

reproducibility of results. The testing procedure followed standard laboratory practices for compression testing of cementitious materials, with attention to specimen alignment, surface leveling, and load application to maintain accuracy and repeatability.

2.3 Method for Multiscale Numerical Modeling and Simulation of Concrete Cylinders Confined by a Sandwich System with Continuous Carbon Fiber–Reinforced Auxetic Core and CFRP Face Sheets

A comprehensive multiscale numerical framework was developed to simulate the behavior of concrete cylinders confined by a sandwich composite system composed of a continuous carbon fiber–reinforced auxetic core and carbon fiber–reinforced polymer (CFRP) face sheets. This integrated approach combines microscale material homogenization, mesoscale cellular modeling, and macroscale structural simulation to capture material interactions and confinement mechanisms under compressive loading.

Microscale Modeling of Continuous Carbon Fiber–Reinforced TPU Composite

At the microscale level, the focus was on characterizing the effective mechanical properties of the auxetic core material, consisting of thermoplastic polyurethane (TPU) reinforced with continuous carbon fibers (CCF). A representative volume element (RVE) was developed to capture the local interactions between the polymer matrix and reinforcing fibers. The RVE dimensions were determined through sensitivity analysis to ensure size independence of the computed homogenized properties. The TPU matrix was modeled as a hyperelastic material using an Ogden model of order three to accurately represent its nonlinear elastic behavior. Material parameters for TPU, including an elastic modulus of approximately 51 MPa and a Poisson's ratio of 0.48, were used to define the hyperelastic response. The carbon fibers were modeled as transversely isotropic with a longitudinal elastic modulus of 780 GPa, a transverse modulus of 10 GPa, and a Poisson's ratio of 0.2. Periodic boundary conditions were applied on all faces of the RVE to ensure continuity between opposing surfaces. A uniaxial strain was applied in one direction while maintaining zero displacement on the orthogonal planes. The resulting stress field was volume-averaged to obtain the effective mechanical response. The homogenized elastic constants and hyperelastic coefficients derived from the RVE were then used to define the constitutive behavior of the auxetic core at the mesoscale level.

Mesoscale Modeling of the Re-entrant Honeycomb Auxetic Core

At the mesoscale, the homogenized composite material from the microscale analysis was used to model the re-entrant honeycomb auxetic core. The re-entrant geometry, characterized by its negative Poisson's ratio, was selected for its ability to provide enhanced confinement and lateral expansion under compressive loading. The geometry of the unit cell was parameterized by the vertical cell length, slant cell length, wall thickness, and re-entrant angle. These parameters were varied systematically to investigate their influence on the mechanical performance and the extent of the auxetic effect. The core material was modeled using the homogenized TPU/CCF properties, which combine flexibility from the polymer matrix and strength from the embedded carbon fibers.

Boundary conditions were defined to simulate a single layer of periodic cells subjected to uniform compressive loading. The load was applied quasi-statically, and lateral expansion was allowed to

occur freely to capture the auxetic deformation response. The finite element model was solved using Abaqus CAE, employing reduced-integration hexahedral elements to ensure computational efficiency and numerical stability. This mesoscale modeling stage provided the effective deformation characteristics, including the equivalent stiffness and Poisson's ratio of the auxetic core, which were then transferred to the macroscale simulation of the sandwich-confined concrete cylinder.

Macroscale Modeling of the Sandwich-Confined Concrete Cylinders

At the macroscale, the full concrete cylinder confined by the sandwich system was modeled to evaluate the global mechanical performance under axial compression. The sandwich system consisted of an inner and outer CFRP face sheet enclosing a middle layer of the carbon fiber–reinforced auxetic core. The concrete cylinder was modeled using the Concrete Damage Plasticity (CDP) model to represent both tensile cracking and compressive crushing. The parameters of the CDP model, including dilation angle, eccentricity, viscosity, and the ratio of biaxial to uniaxial compressive yield stress, were selected based on literature values representative of normal-strength concrete. This model captured the nonlinear inelastic behavior of concrete and its progressive damage evolution under load. The auxetic core was assigned the homogenized material properties obtained from the mesoscale analysis, while the CFRP face sheets were modeled as orthotropic materials with principal moduli of elasticity aligned with the fiber direction. The layers were assembled concentrically around the concrete cylinder to form a three-component sandwich structure. The model geometry included surface-to-surface tie constraints between the interfaces of the concrete, auxetic layer, and CFRP sheets to simulate perfect bonding. The bottom surface of the concrete cylinder was fully fixed, while a compressive load was applied to the top surface through a reference node with displacement control to simulate uniaxial loading. Contact conditions with a static friction coefficient of 1.0 were defined to ensure realistic load transfer between interfaces.

Numerical Implementation and Analysis

All simulations were performed in Abaqus CAE, utilizing the implicit solver with nonlinear geometry effects enabled to capture large deformations and contact interactions. A refined mesh was applied along the interfaces to ensure accurate stress distribution and convergence of results. The mesh density was determined through a convergence study that balanced accuracy and computational efficiency. The analysis output included axial stress–strain curves, deformation patterns, and the evolution of plastic strains within the concrete and auxetic layers. These data were post-processed to quantify the confinement efficiency provided by the auxetic–CFRP sandwich system. The numerical framework thus established a multiscale linkage—from material behavior at the microscale to structural performance at the macroscale—providing a robust basis for understanding how auxetic geometry and fiber reinforcement jointly enhance the strength and ductility of confined concrete cylinders.

Chapter 3: Results and Discussion

3.1 Evaluating the Auxetic Response of Re-entrant Honeycomb Core

3.1.1 Computational and Experimental Results

The Poisson's ratio from the FEA simulations was compared to the tensile data. Fig. 4 (a)-(e) show the displacement images from the progression of the deformation. The undeformed image of the structure is shown in Fig. 4a. followed by the subsequent deformation history up to the maximum 20 mm displacement in Fig. 4e. The Poisson's ratio evaluated from the three structures with the same geometrical features is -0.367.

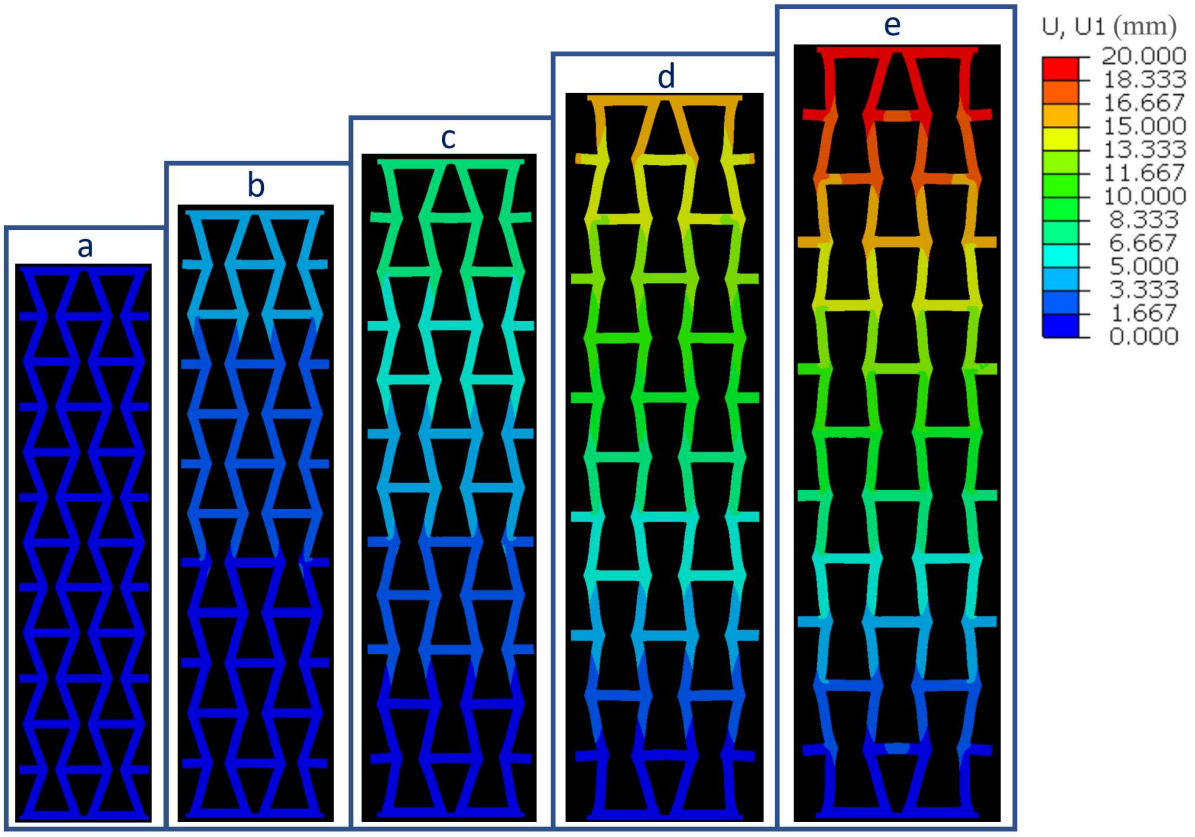

Fig. 9 - Computer numerical simulation images of the selected geometry showing (a) an undeformed shape, (b) 4 mm displacement load, (c) 10 mm displacement load, (d) 16 mm displacement load, (e) and 20 mm displacement load.

For the tensile test/DIC experiment, the entire face of the 3D printed structures, excluding the gripped ends, is selected as the area of interest, as illustrated in Fig. 5a. This selection enables the DIC to compute the strain values to include all the points on the features of the auxetic structures. Fig. 5(b)-(d) show how the auxetic structure increases in dimension transversely with applied uniaxial tension at 5, 10, and 17 mm, respectively. Fig. 5e shows the RT deformed structure at the maximum uniaxial displacement load of 20 mm. The Poisson's ratio evaluated from three replicate

structures with the same geometrical features is -0.372 ± 0.006, which correlates very well with the simulated value. The computational and testing data agree with each other. Hence the simulations are expanded to generate a large dataset to enable machine learning-based performance prediction.

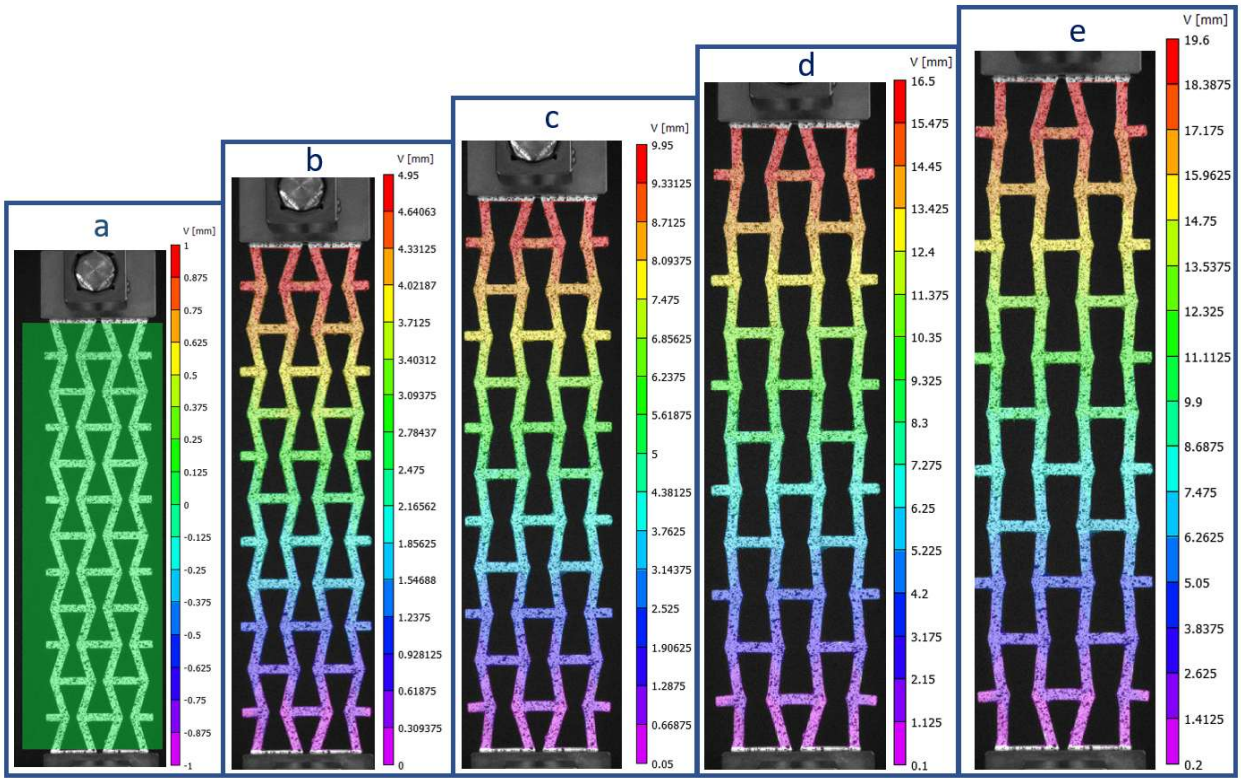

Fig. 10 - DIC images of the selected geometry showing (a) region of interest, (b) deformed sample at 5 mm displacement load, (c)10 mm displacement load, (d) 17 mm displacement load, and (e) 20 mm displacement load.

3.1.2 *Machine Learning Implementation Results*

Dataset Generation and Adequacy

Python scripts containing nested loops of the four geometrical features are loaded in batches into Abaqus CAE scripting to generate 8096 non-self-intersecting re-entrant honeycomb geometries. Each auxetic structure has a uniform re-entrant honeycomb pattern with six repeating units in the horizontal direction and three in the vertical direction. Fig. 6 shows the distribution of datasets of the independent features; (a) slant cell length, (b) cell thickness, (c) vertical cell length in millimeters, and (d) cell angle in degrees, and the dependent feature; (e) Poisson's ratio. To ensure adequacy, four important factors are carefully considered: (a) representativeness, (b) consistency, (c) completeness, and (d) the balanced nature of the dataset.

To ensure representativeness, careful consideration was made so that the dataset contains adequate information for training the model. Toward this, 20% of the whole dataset chosen randomly was kept unseen/hidden, and the remaining 80% data was used for training. Besides, 5-fold cross-

validation was performed to tune the hyperparameters where during each fold, the dataset was further split into an 80% training set and a 20% validation set. Finally, the model was evaluated on the test set to determine the generalizability of unseen input features.

For the completeness and balanced nature of the dataset, all possible combinations of the independent features of the structures were considered in nested loops from the least possible values that yielded non-self-intersecting structures. These values were scaled up uniformly, choosing small step sizes. For example, for the generation of geometries, the minimum slant cell length is 4 mm, and the minimum cell angle of 30^o is adopted. Any angle less than 30^o at a step size of 5^o, when combined with a slant cell length less than 4 mm created a self-intersecting structure. The step size of the slant cell length is 2 mm. For the cell thickness, the minimum cell thickness is 2.0 mm, and step size is 0.2 mm. Cell thicknesses less than 2.0 mm, combined with other geometrical features of any value, created zero thickness element mesh errors for the quadrilateral dominant mesh with the configurations used. The minimum vertical cell length is 25 mm at a step size of 5 mm, for all minimum allowable values for the other three geometrical features. The maximum vertical cell length, slant cell length, cell thickness, and cell angle are 80, 20, 3.4 mm, and 85^o, respectively.

The 8096 different generated structures were each simulated for their Poisson's ratio, following an applied uniaxial displacement load. Fig. 1 shows a schematic illustration of the FEA framework. The numerical simulation of re-entrant honeycomb structures demonstrated that some auxetic structure geometries exhibit a positive Poisson's ratio. 49% of the Poisson's ratios evaluated were equal to or greater than zero, while 51% of the Poisson's ratios evaluated were less than zero. The highest Poisson's ratio of the auxetic structure geometries recorded is 0.23, while the lowest is -0.80.

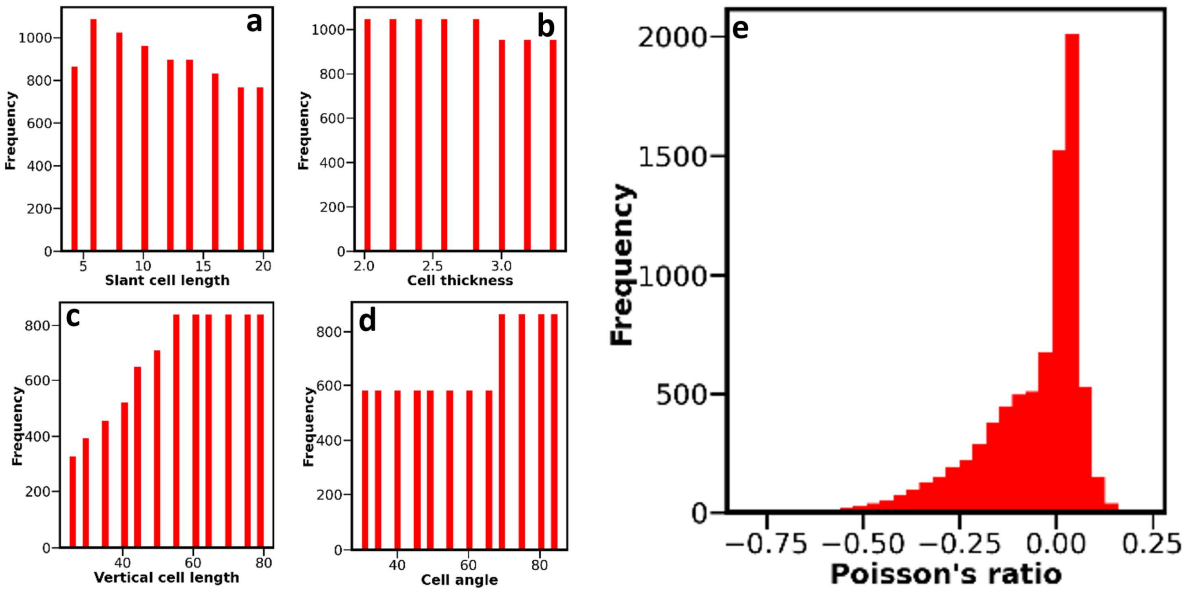

Fig. 11 - Dataset distribution of the independent features; (a) slant cell length, (b) cell thickness, (c) vertical cell length, (d) cell angle, and the dependent feature; (e) Poisson's ratio.

For a detailed evaluation of the generated dataset, the influence of the four geometrical features on the predicted Poisson's ratios is explained in Fig. 7(a)-(f) using surface plots. In Fig. 7a, keeping the slant cell length constant at 12 mm and vertical cell length at 50 mm, the Poisson's ratio decreased from 0.06 to -0.26 when the cell angle was reduced from 80 to 50º. However, the trend reverses beyond 50º, and the Poisson's ratio increases to -0.03 as the angle approaches 30º. The lowest Poisson's ratio of -0.26 was obtained for a cell thickness of 2.0 mm. At a constant slant cell length of 12 mm and cell angle of 55º in Fig. 7b, the Poisson's ratio increased with an increase in cell thickness from 2.0 to 3.4 mm, and an increase in vertical cell length from 45 to 80 mm.

The Poisson's ratios are not significantly affected by the cell thickness and slant cell length, as it can be seen in Fig. 7c. At a constant vertical cell length of 50 mm and cell angle of 55º, the Poisson ratio hovered from 0.03 to 0.06, as the cell thickness decreased from 3.0 to 2.0 mm. The least Poisson's ratio is recorded at a slant cell length of 4 mm. In Figure 7d, the vertical cell length is pegged at 50 mm, and cell thickness is kept constant at 2.6 mm, whereas the slant cell length and angle varied. As it can be seen in Fig. 7d, Poisson's ratio remains unaffected by the variations in the cell angle for lower slant cell length values. However, at higher slant cell length values (beyond 16 mm), the Poisson's ratio significantly decreases as the cell angle is reduced from 80 to 50º.

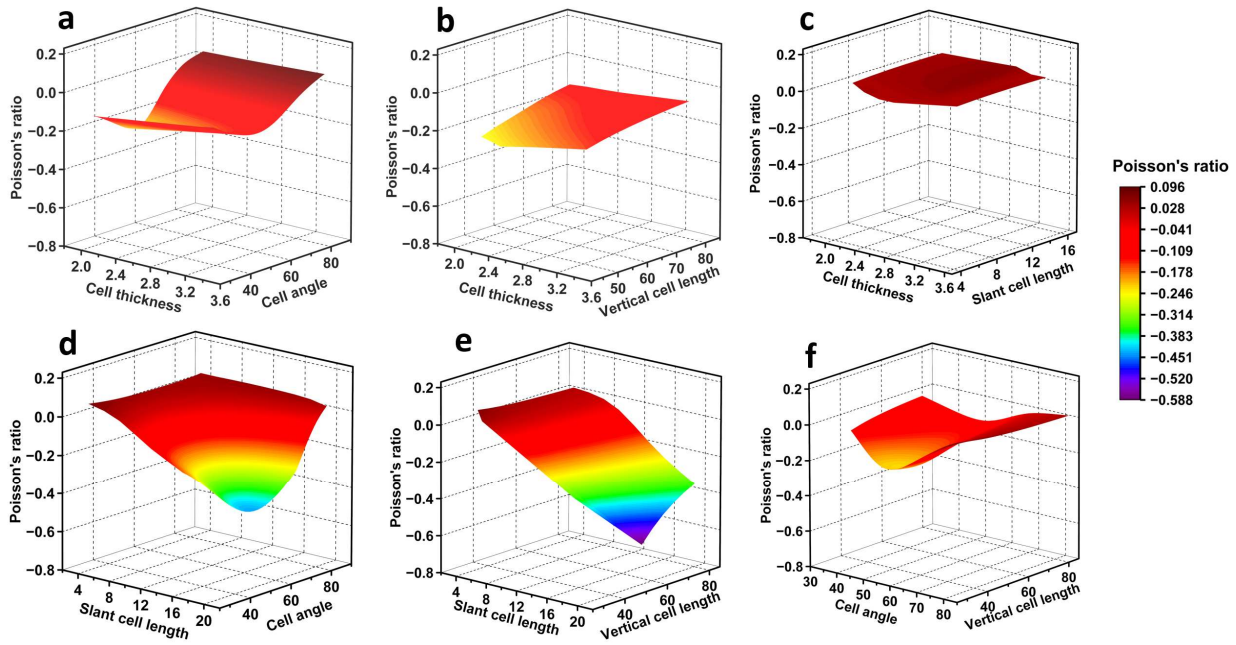

Fig. 12 - Influence of parametric interactions on the Poisson's ratio prediction: (a) cell thickness-cell angle interaction with slant cell length constant at 12 mm and vertical cell length at 50 mm (b) cell thickness-vertical cell length interaction with constant slant cell length of 12 mm and cell angle of 55º, (c) cell thickness-slant cell thickness interaction with constant vertical cell length of 50 mm and cell angle of 55º, (d) slant cell length-cell angle interaction with constant vertical cell length of 50 mm and cell thickness of 2.6 mm, (e) cell angle-vertical cell length interaction with cell thickness and cell angle constant at 2.6 mm and 55º respectively, and (f) slant cell length-vertical cell length interaction for a constant slant cell length of 12 mm and the cell thickness of 2.6 mm.

The slant cell length and the vertical cell length are varied while keeping the cell thickness and cell angle constant at 2.6 mm and 55º in Figures 7e and 7d, respectively. Here, the Poisson's ratio decreases from 0.10 to -0.59 as the slant cell length increases from 4 to 20 mm, while the vertical cell length of 55 mm shows the lowest Poisson's ratio of -0.59. Keeping the slant cell length constant at 12 mm and the cell thickness at 2.6 mm (Fig 5f), the Poisson's ratio decreases from 0.10 to -0.23, as the cell angle is reduced from 80 to 50º but increases to -0.05 as the angle is reduced beyond 50º towards 30º. The vertical cell length shows a relatively lower influence on the predicted Poisson's ratios. Overall, slant cell length-cell angle and slant cell length-vertical cell length interactions significantly influence the negative Poisson's ratios compared to other parametric interactions, which are further explored later in this paper using interpretable machine learning.

Machine Learning Model

Tensorflow [1] ML system with Python is used for training the NN, due to its ability to run on multicore CPU and GPU. Optimization of the weights and the biases is accomplished by determining the model's loss function using the Adam algorithm through backpropagation. In order to optimize the performance of the NN model in this study, a thorough hyperparameter tuning process was considered. This involved carefully considering several hyperparameters, including the learning rate, number of epochs, number of hidden layers, and number of hidden nodes in each layer. MSE and R^2 values were employed to inform the selection of the optimum hyperparameters while balancing computational resources and model efficiency. The hyperparameter tuning process identified five neurons as the most efficient choice to balance model accuracy and computational resources. This conclusion was supported by the MSE and R^2 plot. Furthermore, a learning rate of 0.001 was obtained based on the learning rate sensitivity study. Overall, after the tuning process, we obtained the optimal hyperparameters for our model, which include a learning rate of 0.001, number of epochs of 200, number of hidden layers of 2, and number of neurons of 5. Such a hyperparameter tuning process helps to optimize the performance of the NN model and enables accurate predictions while minimizing computational resources.

The first operation that is conducted on the datasets to prevent overfitting is splitting the dataset into training datasets, and test datasets using Scikit learn library [2] in the ratio of 80:20. The 20% test dataset is kept hidden from the model during training, leaving the 80% only to be exposed and used for model training. At the end of the training, the hidden test dataset is revealed to evaluate the performance of the NN model. The model is trained with k-fold cross-validation (CV) [3]. The R^2 and MSE values deduced from each fold of the CV operation are averaged to evaluate the performance of the NN algorithm. A 5-fold CV on the training dataset enabled the dataset to be reshuffled to a dataset of 80% training and 20% validation [4].

Predicted Machine Learning Results

The performance of the NN model is determined by comparing the FEA-measured Poisson's ratios with the predicted Poisson's ratios data for the training, validation, and test datasets in Fig. 8. The R^2 values for the train, validation, and test datasets is 0.98.

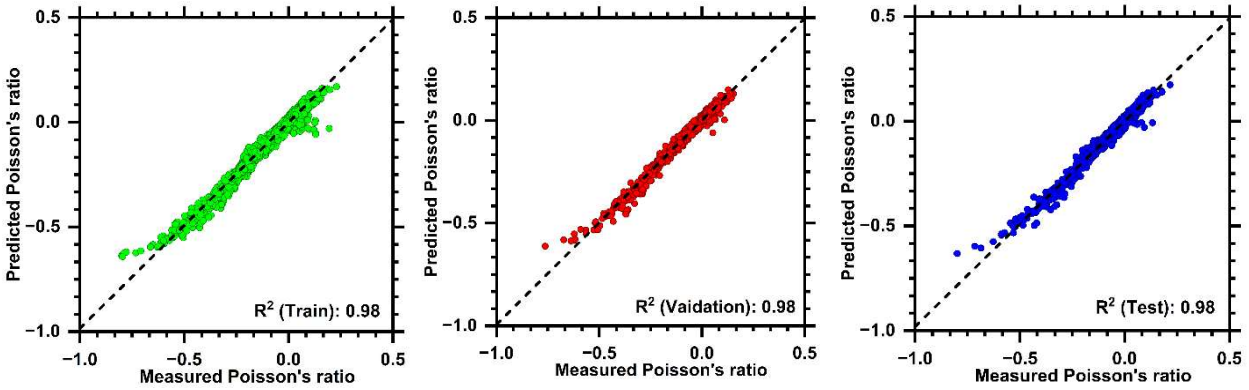

Fig. 13 - Comparison of the measured Poisson's ratio from the FEA model with the predicted Poisson's ratio from the trained NN model using (a) train set, (b) validation set, and (c) test set of data.

SHAP Interpretation of the Predictions

In this section, the SHAP analysis is presented to provide more insight into the predicted Poisson's ratio and to clarify the relative importance of the slant cell length, cell angle, vertical cell length, and cell thickness. The relevance of the individual input features and the influence on the output feature are addressed by assigned importance values. Slant cell length and cell angle strongly influence the prediction of Poisson's ratios relative to the vertical cell length and the cell thickness. As it can be seen in Fig. 9, the Poisson's ratio prediction is dominated by the slant cell length with an absolute SHAP value of 0.08, followed by the cell angle with a SHAP value of 0.07, the vertical cell length with a SHAP value of 0.02, and the cell thickness with a SHAP value of 0.01.

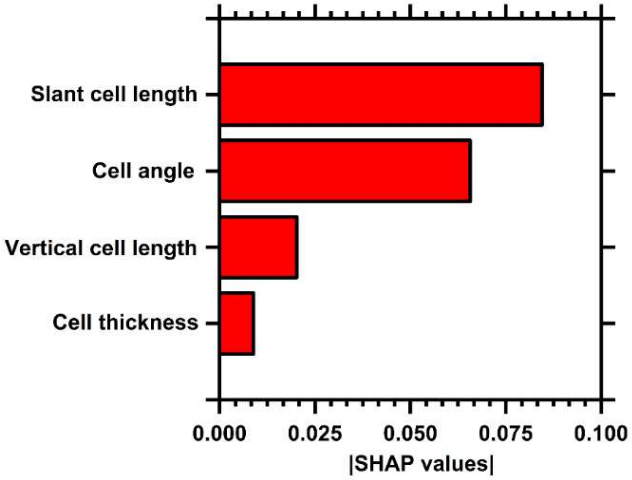

Fig. 14 - SHAP summary plot for the Poisson's ratio for each input from the trained NN model.

To elucidate more on the relative importance of the input features, Fig. 10 shows the violin plots of the SHAP values for the individual input features that contributed to the prediction of the Poisson's ratios. The color scale from blue to red shows the range of values of the individual input feature, and the horizontal axis shows the SHAP values. While the red color represents the highest input feature value, the blue color represents the lowest value of the input feature. The mean

Poisson's ratio of the entire datasets at -0.06 is represented by a SHAP value of zero. The features from top-down are arranged in descending order of importance.

Blue cluster toward the positive SHAP value axis of the slant cell length indicates that the SHAP values corresponding to Poisson's ratios greater than -0.06 correlate to low slant cell length values. A mix of a blue and red cluster from 0 to -0.2 SHAP values depicts that a mix of low and high slant cell length values correspond to the Poisson's ratios less than -0.06. SHAP values from -0.2 to -0.4 with the bold red line indicate that further negative Poisson's ratios less than -0.06 correlate to high slant cell length values. The observed relationship between slant cell length and Poisson's ratios, where increased slant cell length corresponds to decreased Poisson's ratio values and vice versa. The red cluster from -0.07 to 0.28 on the cell angle SHAP violin shows that a small portion of the Poisson's ratio less than -0.06 and a large portion greater than -0.06 was predicted by high cell angle values. An inconsistent mix of red and blue clusters from -0.07 to -0.25 SHAP value depicts that a mix of low and high cell angle values predicted some negative Poisson's ratios. Red clusters from -0.03 to 0.1 SHAP values on the vertical cell length indicate that the quantity of Poisson's ratio from slightly below -0.06 up to the Poisson's ratios that correspond to the SHAP value of 0.1 was predicted by high vertical cell length values. From -0.03 to -0.07 SHAP values, the mix of blue and red indicates that a mix of low and high vertical cell length values predicted the corresponding Poisson's ratios below -0.06. From -0.07 to -0.18 SHAP values on the vertical cell length, the blue clusters depict that low vertical cell length values predicted the negative Poisson's ratios in the cluster.

Cell thickness is a feature that has contributed the least to the prediction of Poisson's ratios. All the SHAP values are within the weak negative correlation of -0.1 and weak positive correlation of 0.1. A cluster of Poisson's ratios is observed corresponding to a SHAP value of zero, and these mean Poisson's ratios around -0.06 are obtained for higher cell thickness values. In fact, most high cell thickness values yield Poisson's ratios equal to or higher than -0.06. However, Poisson's ratios lower than -0.06 are also observed for higher cell thickness values. Results in Fig. 6 corresponding to cell thickness also indicate that lower cell thickness values always yield negative Poisson's ratios lower than -0.06. Hence, although cell thickness shows the least SHAP value (Fig. 9), the violin plot depicts that a judicious selection of lower cell thickness in the design of re-entrant honeycomb structures can provide substantial means to obtain an auxetic response. Overall, comparison of the SHAP violin plot trends and FEA trends reveals a generally good alignment between the two, indicating that the SHAP interpretations are consistent with the fundamental laws of physics. This observation highlights that the interpretable ML model, developed using a dataset generated through fundamental physics-based FEA, not only achieves outstanding predictive efficacy but also maintains the integrity of the underlying fundamental physics.

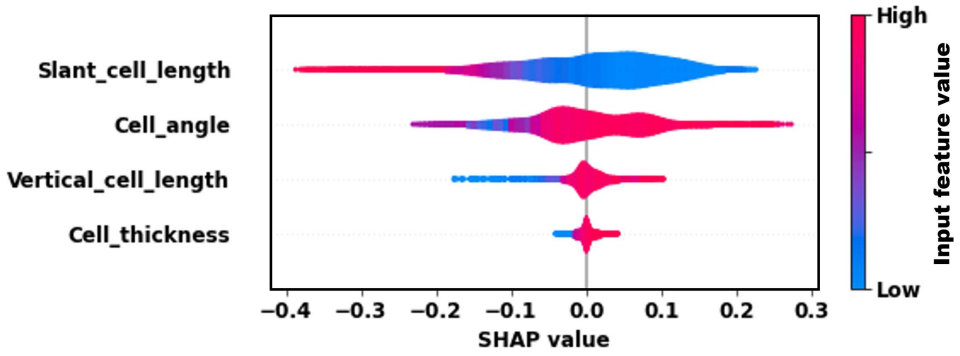

Fig. 15 - SHAP violin plot for the Poisson's ratio using the trained NN model

While the SHAP violin plot concentrates on the impact of a selected individual input feature on the prediction of the Poisson's ratios, the SHAP river flow plot, shown in Fig. 11, concentrates on the impact of the different input features on a selected Poisson's ratio [5]. The SHAP river flow plot of the NN model is illustrated in Fig. 11 for the individual Poisson's ratios, as the four input features influence them. Here, the expected value of -0.06, indicates that the predicted value from the model would be the mean of all the 8096 Poisson's ratios in the training of the NN model when no information on the input feature values is available. Every line of the SHAP river flow plot corresponds to a specific Poisson's ratio. The tendency of these Poisson's ratio lines to sway above or below the expected value line is influenced by the value of the input feature in the model. The color spectrum corresponds to the property value for a given data point. While the red color represents low Poisson's ratio configuration, the blue represents high Poisson's ratio cases. Each predicted Poisson's ratio progressed through the effect of the input features as indicated on the Poisson's ratio axis on the left side of the plot.

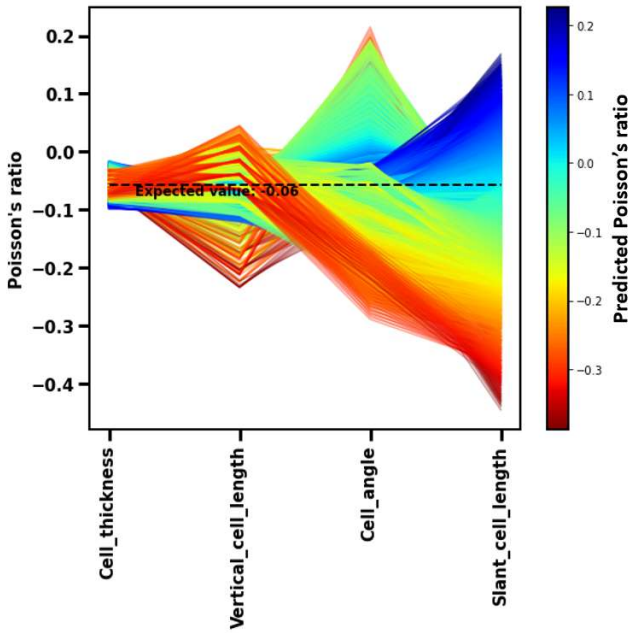

Fig 16 - SHAP river flow plot for Poisson's ratio using the trained NN model

The order of arrangement of the input features from right to left on the horizontal axis is in decreasing absolute SHAP values. Figure 11 shows a clear trend for the slant cell length. The slant cell length decreases the model predictions for low Poisson's ratio configurations. On the other hand, for high Poisson's ratio cases, the slant cell length increases the model predictions. Observation of such a clear trend signifies that slant cell length plays a dominant role in dictating the model output. It is not influenced significantly by the other input features. A mixed trend is observed for both cell angle and vertical cell length. These parameters increase or decrease the model output for low Poisson's ratio configurations. Such a mixed trend indicates that other input features significantly influence the model output for both cell angle and vertical cell length in the model. The trend concerning cell thickness also shows a mixed response. However, the overall variations are relatively narrow. The model output hovers around the expected mean value for changes in cell thickness. Overall, in this study, both SHAP violin and SHAP riverflow plots were implemented to explain the impact and relevance of geometrical features on Poisson's ratios and vice versa. SHAP violin allowed for the identification of the key geometrical features that influenced the prediction of Poisson's ratios, while SHAP river flow explored the influence of different input features on each Poisson's ratio. Thus, synergistic implementation of these two metrics facilitates a comprehensive understanding of the behavior of the NN model and its relationship with the input features. This study primarily focused on the linear elastic response under small displacements, where a constant Poisson's ratio was assumed. It should be noted, however, that under large deformations, the evaluation of strain-dependent Poisson's ratios may be necessary, presenting an interesting avenue for future research.

3.2 Experimental and Numerical Evaluation of 3D-Printed Auxetic Confinement for Cementitious Mortar Cylinders

The experimental results demonstrated that re-entrant auxetic confinement significantly enhanced the compressive strength of mortar specimens compared to unconfined controls. The improvement in strength is attributed to the negative Poisson's ratio behavior of auxetic structures, which exert lateral compression on the mortar as the axial load increases. Among the three materials tested, ABS confinement exhibited the highest strength increase due to its superior stiffness and balanced ductility. PLA confinement also produced substantial gains, while TPU showed moderate improvement because of its compliant nature. The average compressive strength results for all configurations are summarized in Table 1.

The results clearly show that auxetic confinement enhances the compressive performance of cementitious mortar. The ABS-confined specimens exhibited the highest average compressive strength of 45.7 MPa, representing a 34% increase over the unconfined control. PLA confinement achieved a 24% strength improvement, while TPU confinement yielded an 11% increase. These outcomes confirm that auxetic confinement mechanisms, particularly with stiffer polymers, provide significant enhancement in load-bearing capacity suitable for structural strengthening applications.

Table 1. Average compressive strength of mortar specimens with different confinement materials.

Control (Unconfined)	—	34.2	—
Auxetic–PLA	Polylactic Acid (PLA)	42.5	24%
Auxetic–ABS	Acrylonitrile Butadiene Styrene (ABS)	45.7	34%
Auxetic–TPU	Thermoplastic Polyurethane (TPU)	38.1	11%

Finite element simulations were carried out using Abaqus CAE to evaluate the compressive behavior of cementitious mortar cylinders confined by 3D-printed re-entrant auxetic geometries made from different polymer materials. The simulations replicated the experimental configuration to assess load-bearing performance and confinement efficiency. The mortar was modeled using the Concrete Damage Plasticity (CDP) model to capture its nonlinear compressive response. The auxetic shells were modeled as elastic or hyperelastic solids depending on the confinement material—PLA and ABS were modeled as elastic–plastic materials, while TPU was represented using an Ogden hyperelastic model. The confinement layers were tied to the mortar surface through surface-to-surface contact with perfect bonding assumed. The bottom surface of the cylinder was fully fixed, and a compressive load was applied at the top to simulate uniaxial compression. The simulations were performed using quasi-static loading conditions under the Dynamic Explicit scheme to ensure numerical stability. The ratio of kinetic to internal energy remained below 5%, validating the quasi-static nature of the simulation.

The numerical simulations accurately reproduced the compressive behavior of the confined mortar specimens and provided close agreement with experimental findings. Predicted compressive strength values were within ±2% of measured data, confirming the reliability of the adopted modeling framework. As observed experimentally, auxetic confinement significantly enhanced the load-bearing capacity of the specimens. ABS confinement yielded the highest predicted strength, followed by PLA and TPU, mirroring the experimental trends. Table 2 presents the simulated compressive strength results and their deviation from experimental values.

The simulation results confirmed that the auxetic confinement geometry effectively enhances the compressive strength of cementitious mortar cylinders. The ABS auxetic shell exhibited the highest strength enhancement, consistent with the experimental findings. The strong correlation between simulated and measured values validates the numerical model and demonstrates its potential for predictive evaluation and parametric studies of auxetic confinement systems.

Table 2. Simulated compressive strength results for auxetic-confined mortar specimens.

Auxetic–PLA	Polylactic Acid (PLA)	43.1	+1.4
Auxetic–ABS	Acrylonitrile Butadiene Styrene (ABS)	46.4	+1.5
Auxetic–TPU	Thermoplastic Polyurethane (TPU)	37.4	–1.8

3.3 Numerical Results: Concrete Cylinders Confined with TPU–Continuous Carbon Fiber Auxetic Core and CFRP Wraps

In the previous study, thermoplastic polyurethane (TPU) auxetic confinement showed the least enhancement in compressive strength among the printed polymeric materials tested. This was primarily attributed to TPU's high flexibility and low stiffness, which limited its ability to impose strong lateral confinement during loading. However, TPU's compliant nature presents a key advantage for practical applications at structural scales—its inherent elasticity allows for tight, conformal fitting around irregular concrete surfaces, ensuring effective contact and uniform stress transfer when applied to bridge columns and other cylindrical components. Building on this premise, the current study explores how reinforcing TPU with continuous carbon fibers (CCF) and combining it with external carbon fiber reinforced polymer (CFRP) wraps can create a hybrid confinement system that synergizes flexibility, strength, and durability. Specifically, this section presents the performance of hybrid concrete confinement systems combining thermoplastic polyurethane (TPU)–based re-entrant auxetic (3RE) cores with continuous carbon fiber (CCF) reinforcement and external carbon fiber reinforced polymer (CFRP) wraps.

The compressive strength data (Table 3) reveal a clear enhancement trend across different reinforcement configurations. The unconfined concrete cylinder exhibited a baseline compressive strength of approximately 30 MPa. Wrapping with two CFRP layers (2CFRP) increased strength to about 58 MPa (+93%), while four layers (4CFRP) raised strength to 75 MPa (+120%). The auxetic-only core (3RE, VF=20%) achieved 50 MPa (+67%), confirming confinement effectiveness even without CFRP. The hybrid systems—1CFRP–3RE (VF=20%)–1CFRP and 2CFRP–3RE (VF=20%)–2CFRP—achieved 70 MPa (+214%) and 75 MPa (+221%), respectively, indicating that moderate wrapping densities yield near-optimal confinement performance.

Strain capacity results (Table 4) emphasize the ductility benefits of hybrid confinement systems. Plain concrete showed the lowest strain capacity (0.0020 mm/mm). The 2CFRP and 4CFRP configurations exhibited slight improvements (0.0022 and 0.0024 mm/mm, respectively). The auxetic-only 3RE (VF=20%) specimen achieved 0.0028 mm/mm (+40%), demonstrating the auxetic mechanism's ability to delay failure. Hybrid systems exhibited the largest ductility enhancements: 1CFRP–3RE (VF=20%)–1CFRP reached 0.0035 mm/mm (+75%), and 2CFRP–

3RE (VF=20%)–2CFRP reached 0.0036 mm/mm (+80%), confirming the synergistic benefit of auxetic and CFRP confinement.

Table 3. Compressive strength of concrete cylinders with different confinement configurations.

Plain Concrete	Unconfined concrete cylinder	30	—
2CFRP	Two layers of CFRP wrap	58	+93%
4CFRP	Four layers of CFRP wrap	75	+120%
3RE (VF=20%)	Three-layer auxetic core with 20% CCF	50	+67%
1CFRP–3RE (VF=20%)–1CFRP	Hybrid sandwich with one CFRP layer on each side	70	+214%
2CFRP–3RE (VF=20%)–2CFRP	Hybrid sandwich with two CFRP layers on each side	75	+221%

Table 4. Strain capacity of concrete cylinders with different confinement configurations.

Plain Concrete	Unconfined concrete cylinder	0.0020	—
2CFRP	Two layers of CFRP wrap	0.0022	+10%
4CFRP	Four layers of CFRP wrap	0.0024	+20%
3RE (VF=20%)	Three-layer auxetic core with 20% CCF	0.0028	+40%
1CFRP–3RE (VF=20%)–1CFRP	Hybrid sandwich with one CFRP layer on each side	0.0035	+75%
2CFRP–3RE (VF=20%)–2CFRP	Hybrid sandwich with two CFRP layers on each side	0.0036	+80%

The results demonstrate that while the contribution of the auxetic core to compressive strength becomes less dominant at higher CFRP confinement levels, its role in enhancing strain capacity and ductility remains substantial. The negative Poisson's ratio behavior of the auxetic core promotes lateral contraction under axial compression, increasing confinement pressure on the

concrete and delaying microcrack formation. When integrated with CFRP face sheets, this lateral contraction also ensures continuous mechanical contact, minimizing debonding and promoting efficient stress transfer across interfaces. Overall, the hybrid TPU–CCF–CFRP system achieves superior load-bearing capacity, ductility, and energy absorption compared to single-material confinement systems. These findings confirm the effectiveness of this dual-mechanism confinement strategy for developing durable, damage-tolerant materials for transportation infrastructure applications.

Chapter 4: Conclusions and Recommendations

This project successfully demonstrated the feasibility and effectiveness of employing 3D-printed auxetic and hybrid composite systems for the structural strengthening of transportation infrastructure. Through an integrated sequence of experimental investigations, numerical simulations, and multiscale modeling, the research established a comprehensive understanding of how auxetic geometries and fiber-reinforced composites can enhance the mechanical performance, confinement efficiency, and overall durability of concrete structures.

The material development and testing confirmed that 3D-printed thermoplastic polyurethane (TPU)–based auxetic geometries provide conformal and flexible confinement to concrete cylinders, enabling improved crack control and delayed failure. Although TPU alone exhibited limited strength enhancement, its unique negative Poisson's ratio behavior and snug fit to the concrete surface make it particularly effective when upscaled for field applications where adaptability and continuity of contact are essential. When integrated with continuous carbon fiber (CCF) reinforcement, the auxetic core exhibited significantly higher compressive strength, demonstrating the benefit of combining flexibility with fiber stiffness. Further enhancement was achieved through the application of external carbon fiber reinforced polymer (CFRP) wraps, producing a multilevel confinement system capable of substantial gains in strength and ductility.
The simulation and machine learning–based modeling framework developed in this project provided detailed insights into the behavior of these confinement systems at multiple scales. The multiscale finite element simulations accurately captured stress transfer and confinement efficiency from microscale fiber–matrix interactions to macroscale structural response.

Together, the experimental and computational results demonstrate that hybrid TPU–CCF–CFRP confinement systems offer a promising, adaptable, and scalable solution for strengthening deteriorated or underperforming concrete components in transportation infrastructure. These systems provide improved load-bearing capacity, energy absorption, and crack resistance, while maintaining manufacturability through 3D printing and composite fabrication methods. The combined experimental validation and predictive modeling framework developed in this work establish a scientific and practical foundation for the broader application of advanced auxetic and fiber-reinforced composites in structural rehabilitation and resilience enhancement.

Looking forward, the methodology and findings from this project pave the way for full-scale testing, long-term durability studies, and design integration into standard rehabilitation practices. The demonstrated synergy between experimental validation, numerical simulation, and intelligent modeling provides a rational, data-driven basis for developing next-generation strengthening materials tailored to the evolving demands of modern transportation infrastructure.

References

[1] Abadi M, Barham P, Chen J, Chen Z, Davis A, Dean J, et al. TensorFlow: A system for large-scale machine learning 2016.

[2] Naji MA, Filali SE, Aarika K, Benlahmar EH, Abdelouhahid RA, Debauche O. Machine Learning Algorithms For Breast Cancer Prediction And Diagnosis. 18th Int Conf Mob Syst Pervasive Comput MobiSPC 16th Int Conf Future Netw Commun FNC 11th Int Conf Sustain Energy Inf Technol 2021;191:487–92. https://doi.org/10.1016/j.procs.2021.07.062.

[3] Cawley GC, Talbot NLC. On over-fitting in model selection and subsequent selection bias in performance evaluation. J Mach Learn Res 2010;11:2079–107.

[4] Yang K, Xu X, Yang B, Cook B, Ramos H, Krishnan NMA, et al. Predicting the Young's Modulus of Silicate Glasses using High-Throughput Molecular Dynamics Simulations and Machine Learning. Sci Rep 2019;9:8739. https://doi.org/10.1038/s41598-019-45344-3.

[5] Bhattoo R, Bishnoi S, Zaki M, Krishnan NMA. Revealing the Compositional Control of Electrical, Mechanical, Optical, and Physical Properties of Inorganic Glasses. 2021.

Transportation Infrastructure Durability Center
AT THE UNIVERSITY OF MAINE

35 Flagstaff Road
Orono, Maine 04469
tidc@maine.edu
207.581.4376

www.tidc-utc.org